Plasma Phys. Control. Fusion **51** (2009) 055020 (15pp) doi:10.1088/0741-3335/51/5/055020

Studies of blob formation, propagation and transport mechanisms in basic experimental plasmas (TORPEX and CSDX)*

S H Müller[1,2], C Theiler[1], A Fasoli[1], I Furno[1], B Labit[1], G R Tynan[2], M Xu[2], Z Yan[2] and J H Yu[2]

[1] Centre de Recherches en Physique des Plasmas, Association EURATOM–Confédération Suisse, CRPP EPFL, Lausanne, Switzerland
[2] Center for Energy Research, University of California, San Diego, CA-92093, USA

E-mail: shmuller@ucsd.edu

Received 2 June 2008, in final form 17 March 2009
Published 9 April 2009
Online at stacks.iop.org/PPCF/51/055020

Abstract

The findings of previous blob studies in the interchange-dominated regime of TORPEX helium (Müller *et al* 2007 *Phys. Plasmas* **14** 110704) and hydrogen plasmas (Furno *et al* 2008 *Phys. Rev. Lett.* **100** 055004) are summarized and compared. The onset of blobs is studied as a function of the vertical magnetic field B_z, proving the existence of blobs also in the drift-interchange-dominated regime characterized by $B_z < 1$ mT. These blobs, despite being inherently three-dimensional and sheath-disconnected, exhibit statistical properties similar to the blobs in the interchange regime. Using conditionally averaged density and potential measurements, the entire time line of an interchange instability leading to the formation of wave-like structure patterns and blobs could be experimentally observed. These results show that a background $\boldsymbol{E} \times \boldsymbol{B}$ shear flow is not essential for the generation of blobs and that the phase shift between density and potential during the generation of blobs is $\pi/2$ in all studied cases, demonstrating the interchange nature of blobs in TORPEX. Fast-camera and Langmuir probe measurements of blobs in the linear device CSDX (Tynan *et al* 2004 *Phys. Plasmas* **11** 5195) support the hypothesis that an interchange instability is also responsible for the generation of blobs in the linear geometry, where the necessary effective gravity is provided by centrifugal forces.

(Some figures in this article are in colour only in the electronic version)

* Paper from the 35th EPS Conference on Plasma Physics (Hersonissos, Crete, Greece, 9–13 June 2008).

1. Introduction

Plasma blobs, i.e. isolated, propagating structures of increased plasma density, have been found and studied in the plasma edge and scrape-off-layers (SOLs) of magnetic-fusion devices [1, and references therein] and in a wide range of basic experiments [2–6]. Many models and simulation approaches have been developed to describe the generation, propagation and transport properties of such blobs [7–16 and references therein], which need to be experimentally validated. First steps toward a large-scale experimental validation of such global edge turbulence codes have been taken successfully for linear devices [17, 18], but much remains to be done, motivating this work of blob studies in basic toroidal and linear experiments.

In the basic toroidal device TORPEX (major radius $R = 1\,\mathrm{m}$, minor radius $a = 0.2\,\mathrm{m}$) [19], hydrogen, helium and argon plasmas are produced at the electron cyclotron (EC) and upper hybrid (UH) resonances by RF waves at 2.45 GHz [20]. A small vertical component of $B_z < 4\,\mathrm{mT}$ is superimposed onto the toroidal magnetic field of $B_\varphi \sim 76\,\mathrm{mT}$ [21]. Despite its small magnitude, B_z plays an important role as an experimental control parameter via its action on the magnetic topology [22], defining the distance $\Delta \equiv 2\pi R(B_z/B_\varphi)$ between two points in the poloidal plane connected by the same field line, and the connection length $L \equiv 2a(B_\varphi/B_z) = 2\pi R(2a)/\Delta$. Typical densities and electron temperatures for hydrogen, helium and argon are, respectively, $n \sim \{3, 3, 10\} \times 10^{16}\,\mathrm{m}^{-3}$, $T_\mathrm{e} \sim \{4, 7, 3.5\}\,\mathrm{eV}$, with peak values about twice as high. Other relevant parameters are $c_s \sim \{20, 10, 3\}\,\mathrm{km\,s}^{-1}$, $\rho_s \equiv c_s/\omega_{ci} \sim \{3, 7, 15\}\,\mathrm{mm}$, $\lambda^{ei}_\mathrm{mfp} \sim \lambda^{en}_\mathrm{mfp} = \mathcal{O}(1)\,\mathrm{m}$. Two general turbulent scenarios are distinguishable in TORPEX based on the dominant instabilities [23], namely the *interchange* scenario for $B_z > 1\,\mathrm{mT}$, or $\Delta > 8\,\mathrm{cm}$, and the *drift-interchange* scenario for $B_z < 1\,\mathrm{mT}$, or $\Delta < 8\,\mathrm{cm}$. The former is characterized by slab-like profiles and features turbulence with a largely two-dimensional character, while in the latter the profiles lose the slab-like character and three-dimensional drift-wave dynamics become important.

In [24], a configuration has been identified in TORPEX, in which blobs have been found to propagate from the main plasma into a source-free, SOL-like region. For this configuration, a helium plasma with $\Delta = 13.6\,\mathrm{cm}$, the blobs were related to field-aligned structures generated in the core plasma, which appear in the perpendicular plane as a wave-like pattern with $k_z = 2\pi/\Delta$. This wave structure travels vertically upward at speeds of the order of $2\,\mathrm{km\,s}^{-1}$, comparable to the ambient $\boldsymbol{E} \times \boldsymbol{B}$ velocity. It was found that the positive wave crests give rise to blobs, which fully detach from the main plasma and propagate radially outward, leading to very similar signatures in time-series statistics as observed in the tokamak SOL [25–27]. It was suggested that the process of blob generation can be described as a radial elongation of wave crests, whose outer parts lag behind in the vertical motion until detachment of a blob occurs. The use of the HEXTIP probe array [22], which covers the whole poloidal cross section with a hexagonal grid of 86 Langmuir probes, together with the use of a pattern-recognition-based method to identify and track blobs [28], allowed us to directly infer the contribution of blobs to transport. Blobs can be held responsible for up to 10% of the overall device losses in TORPEX [24, 29], despite the fact that the configuration is characterized by open field lines. Inferring to a closed field line situation, this number easily warrants consideration of blobs as a primary mechanism for losses across the separatrix in magnetic-fusion devices.

The mechanism of blob generation in TORPEX was studied further in [30, 31], in which a different plasma configuration than in [24] was used, namely hydrogen instead of helium and a higher vertical field ($\Delta = 19\,\mathrm{cm}$ instead of $\Delta = 13.6\,\mathrm{cm}$). Two-dimensional conditional images in density, plasma potential and temperature were obtained by triggering a scanning swept Langmuir probe from a reference probe in the outer SOL region. It was found that

the observed conditional structure motion follows precisely the instantaneous $\boldsymbol{E} \times \boldsymbol{B}$ velocity, such that the observed shearing-off of blobs from the wave crests can be attributed to shear in the instantaneous $\boldsymbol{E} \times \boldsymbol{B}$ velocity. The radial elongation of the wave crest was attributed to a steepening of the radial pressure gradient. This result was confirmed by a complementary study [32], which also clarified that blobs are fully sheath-connected [12] in the interchange-dominated regime.

The first goal of this paper is to bridge between the configurations studied in [24] and [30–32] (section 2) and to extend the findings into the drift-interchange-dominated regime characterized by $\Delta < 8\,\mathrm{cm}$ [23] (section 3). In the second part of the paper, we demonstrate the interchange nature of blobs for both regimes in TORPEX (section 4) and present data from the linear device CSDX [33, 34] that suggests that this might also be true for the linear geometry (section 5).

2. Blobs in TORPEX in the interchange-dominated regime

Figure 1 compares the previously published cases of {He, $\Delta = 13.2\,\mathrm{cm}$} [24] and {H, $\Delta = 19.4\,\mathrm{cm}$} [30–32] as well as the cases {H, $\Delta = 13.2\,\mathrm{cm}$} and {He, $\Delta = 19.4\,\mathrm{cm}$}. In general, helium and hydrogen plasmas in TORPEX are similar, with the difference that helium is characterized by a significantly higher electron temperature (peak values: $T_\mathrm{e}^\mathrm{He} \sim 14\,\mathrm{eV}$; $T_\mathrm{e}^\mathrm{H} \sim 8\,\mathrm{eV}$). The density profiles in row (*a*) show good similarity between all four cases, with the SOL region roughly identified by $r > 0$. The spatial regions where the interchange wave dominates, shown in row (*b*), also exhibit good agreement, with the difference of significantly higher frequencies in helium than in hydrogen, and decreasing frequencies with increasing Δ (figure 2). The structure-analysis results in row (*c*) are obtained from data sets of a minimum length of 0.6 s (sampled at 250 kHz, low-pass filtered at 30 kHz), using the same parameters as in [24, 28], namely a segmentation threshold of $1 \times \sigma_\mathrm{tot}$ (σ_tot is the square root of the average variance of all measurement signals) and a minimum trajectory length of 30 time frames. While the agreement is still qualitatively good, the relative number of radial to vertical trajectories is significantly lower in hydrogen. This fact translates into a significantly lower fraction of transport caused by blobs (not shown) [29].

Row (*d*) in figure 1 shows the conditionally averaged density, triggered when the signal at $\{r, z\} = \{8.75,\ 3.03\}\,\mathrm{cm}$ exceeds 3.5σ, where σ is the standard deviation. The trigger position is roughly half way across the SOL, such that blobs are captured during or closely after their generation. The conditional snapshots are very similar for hydrogen and helium. Comparing the two Δ cases, a significant qualitative difference becomes obvious: while blobs in the high-Δ case appear to be sheared off a larger structure, in the low-Δ case they appear to result from entire structures moving radially. This will be investigated more closely in section 4.

The direct, non-averaged spatiotemporal sequence of a blob-ejection event, shown in figure 3 for the {He, $\Delta = 13.2\,\mathrm{cm}$} case, confirms that the conditionally averaged sequences and snapshots are sufficiently representative for the system dynamics, but also highlights some aspects that are lost in the averaging procedure, such as the occasional merging between two consecutively ejected blobs (frames 1–6).

3. Blobs in TORPEX in the drift-interchange-dominated regime

In the following, we investigate whether blobs also arise in the drift-interchange-dominated regime characterized by $B_z < 1\,\mathrm{mT}$ or $\Delta < 8\,\mathrm{cm}$ [23]. This regime is characterized by strong modifications of the plasma behavior triggered by minor variations of B_z [22]. It is worth

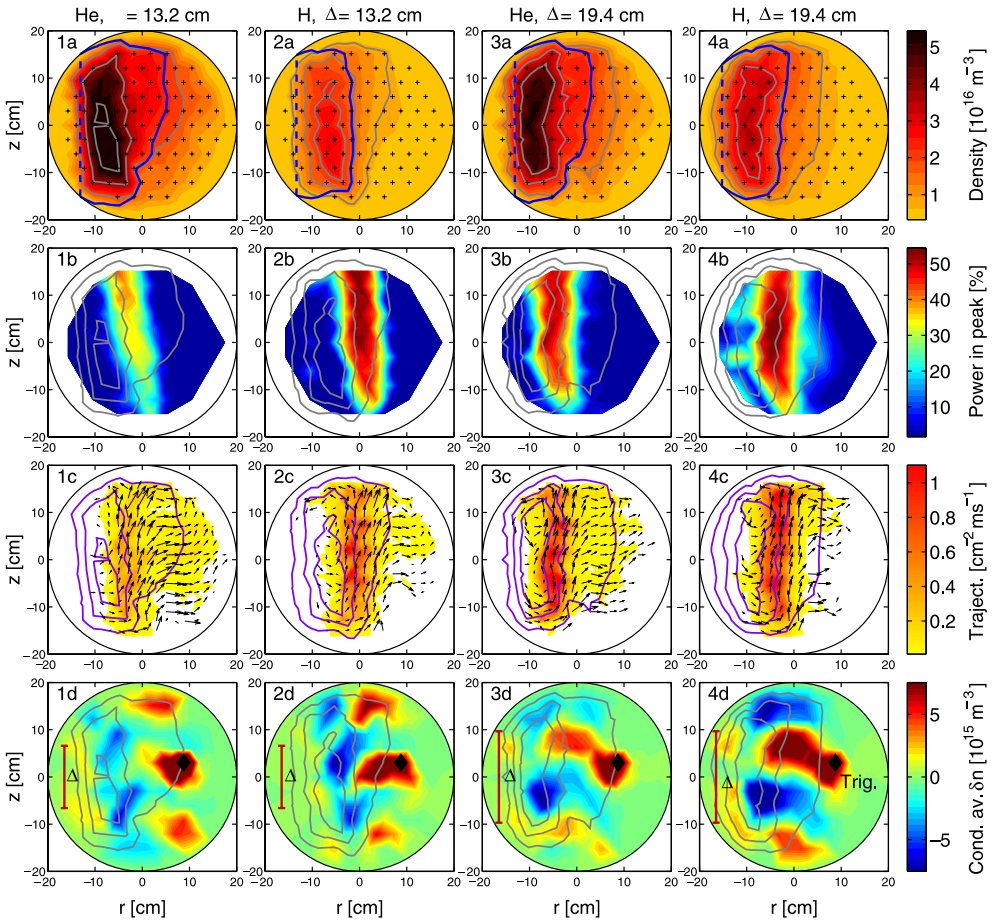

Figure 1. Comparison of helium and hydrogen plasmas in the interchange-dominated regime for the two values of Δ in [24, 30]. (*a*) Time-average density profile with superimposed EC (dashed) and UH resonances. The measurement points are shown as '+' symbols. (*b*) Spatial distribution of spectral power in the dominant spectral region. (*c*) Structure trajectory histogram and flow field for positive structures. (*d*) Conditionally-averaged density triggered when the signal at $\{r, z\} = \{8.75,\ 3.03\}$ cm exceeds 3.5σ. Three contour lines of the time-average density profile are shown in all frames.

noting that the value of B_z at which the transition occurs coincides with the value of B_z for which a simple confinement model predicts the transition from $\boldsymbol{E} \times \boldsymbol{B}$-dominated to sheath-dominated non-turbulent losses [21]. Having established the general similarity of helium and hydrogen plasmas, we restrict the analysis in the following to helium.

Figure 4 shows the analysis of structure trajectories, as in figures 1 (*c*), when Δ is decreased from the interchange regime to the drift-interchange regime. The radial structure trajectories typical for the interchange regime gradually disappear (figures 4(*f*) and (*d*)). After going through a transition (*c*), another configuration characterized by radial structure trajectories is reached (*b*), which disappear again for very low values of Δ (*a*). The background plasma density gradually loses the slab-like character and starts to accumulate in the top section of the vessel. The exact reasons for this are not understood.

A closer examination of the case in figure 4(*b*) reveals that blobs exist also in the drift-interchange regime. Figure 5(*b*) shows a snapshot of an isolated blob structure, which has

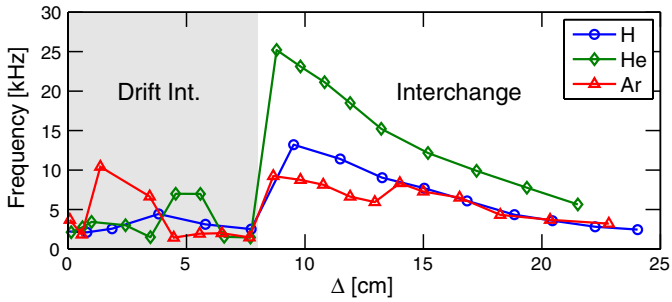

Figure 2. Globally dominant frequency as a function of Δ, showing the change in the dominant mode between the drift-interchange and the interchange regime in hydrogen and helium (argon for completeness). The frequencies of the interchange mode are about twice as high in helium than in hydrogen, which translates back to a higher mean $\boldsymbol{E} \times \boldsymbol{B}$ velocity. The different cross sections for electron-impact ionization for hydrogen and helium lead to about 50% higher electron temperatures in helium [35]. Sheath physics demands that $\phi \sim \Lambda T_e$, $\Lambda \equiv \frac{1}{2} \ln[m_i/(2\pi\, m_e)]$, which explains the higher mean $\boldsymbol{E} \times \boldsymbol{B}$ velocities in helium.

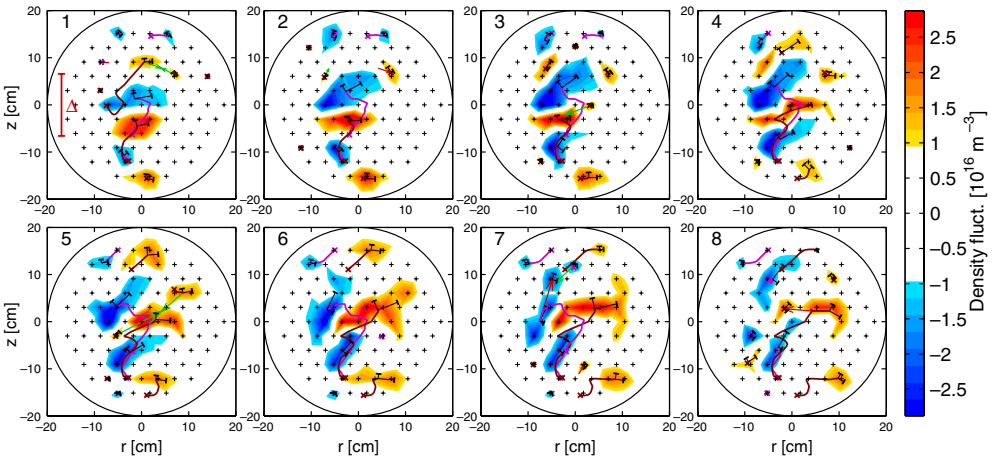

Figure 3. Direct spatiotemporal sequence of a blob-ejection event for the helium case with $\Delta = 13.2\,\mathrm{cm}$ (time resolution: $8\,\mu\mathrm{s}$). Shown are the structures identified by the threshold-segmentation approach and the extracted structure-observables center of mass, extension and orientation ('L' symbols), trajectories (lines) and splitting/merging events (arrows). Immersed into a vertical $\boldsymbol{E} \times \boldsymbol{B}$ background flow [30], positive structures move radially outward while negative structures move inward—the signature of an interchange instability. The negative structures show a significant counter-clockwise tilting, and occasionally two consecutively ejected blobs merge together (frame 5).

undergone a long radial trajectory. In contrast to the blobs in the interchange regime, the vertical dimensions of this blob are larger than Δ, which has two important implications. First, the fact that the same field line passes through the blob structure about twice suggests that short-circuiting effects of the ∇B-induced polarization are active within the blob structure [21]. Second, it is clear that the blob cannot be sheath-connected and that its parallel wavenumber must be different from zero. Motivated by theoretical results [7, 8, 12, 13] suggesting that the parallel boundary conditions in general and sheath-connectedness in particular play an important role for the propagation properties of blobs, the statistical properties of the blobs in the sheath-disconnected and sheath-connected cases are compared in the following.

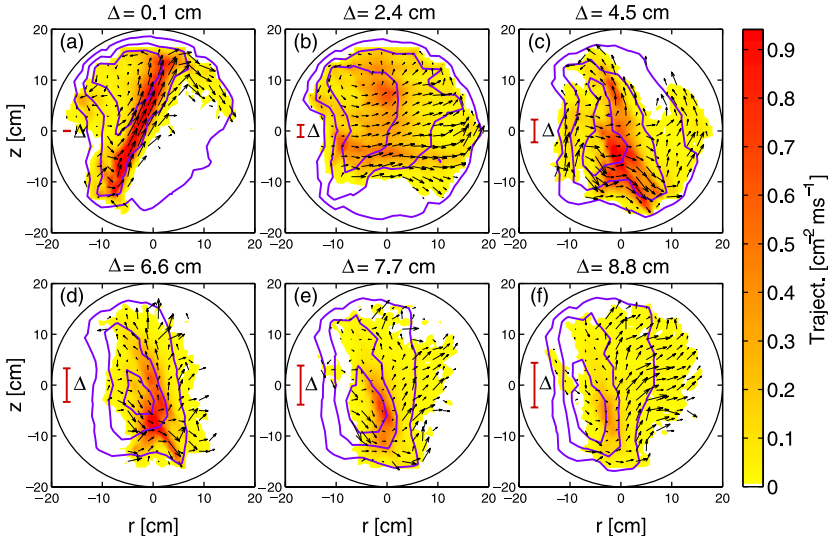

Figure 4. Trajectory analysis in the drift-interchange regime for positive structures for different Δ. The transition to the interchange regime occurs at Δ > 8 cm. The contours represent the time-average density profiles.

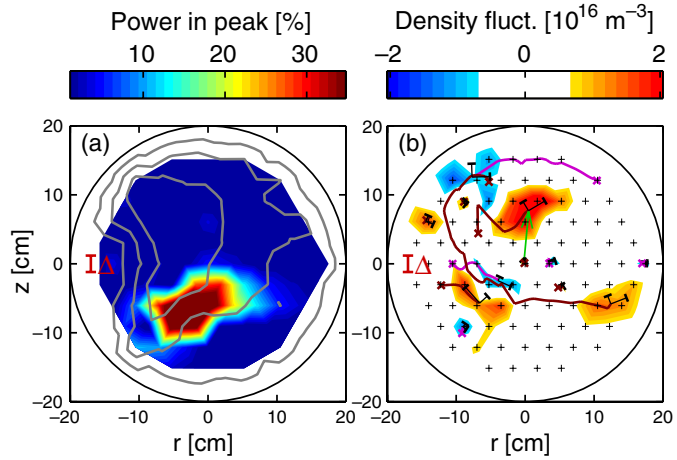

Figure 5. Blobs in the drift-interchange-dominated regime for Δ = 2.4 cm. (*a*) The dominant instability is localized on the low-field side on the bottom of the profile. (*b*) Snapshot of an isolated blob structure encountered far from the main plasma (representation as in figure 3).

Figure 6 presents a side-by-side comparison of the two regimes in terms of results of the statistical analysis of turbulent structures, namely the pilot chart, the death–birth conditional probability, and the transport chart, which are explained in detail in [28] and in appendix A. In the pilot chart in figure 6(*a*), two sets of comparable regions are highlighted, accounting for the different shapes of the density profiles and the different location of the main blob channel, which lies vertically lower in the drift-interchange case (see transport chart in figure 6(*c*), for example). For both regimes, the closer SOL region (full circles) is characterized by a probability of radially-outward motion >70% and by average radial velocities in the 1250–1750 m s^{-1} range.

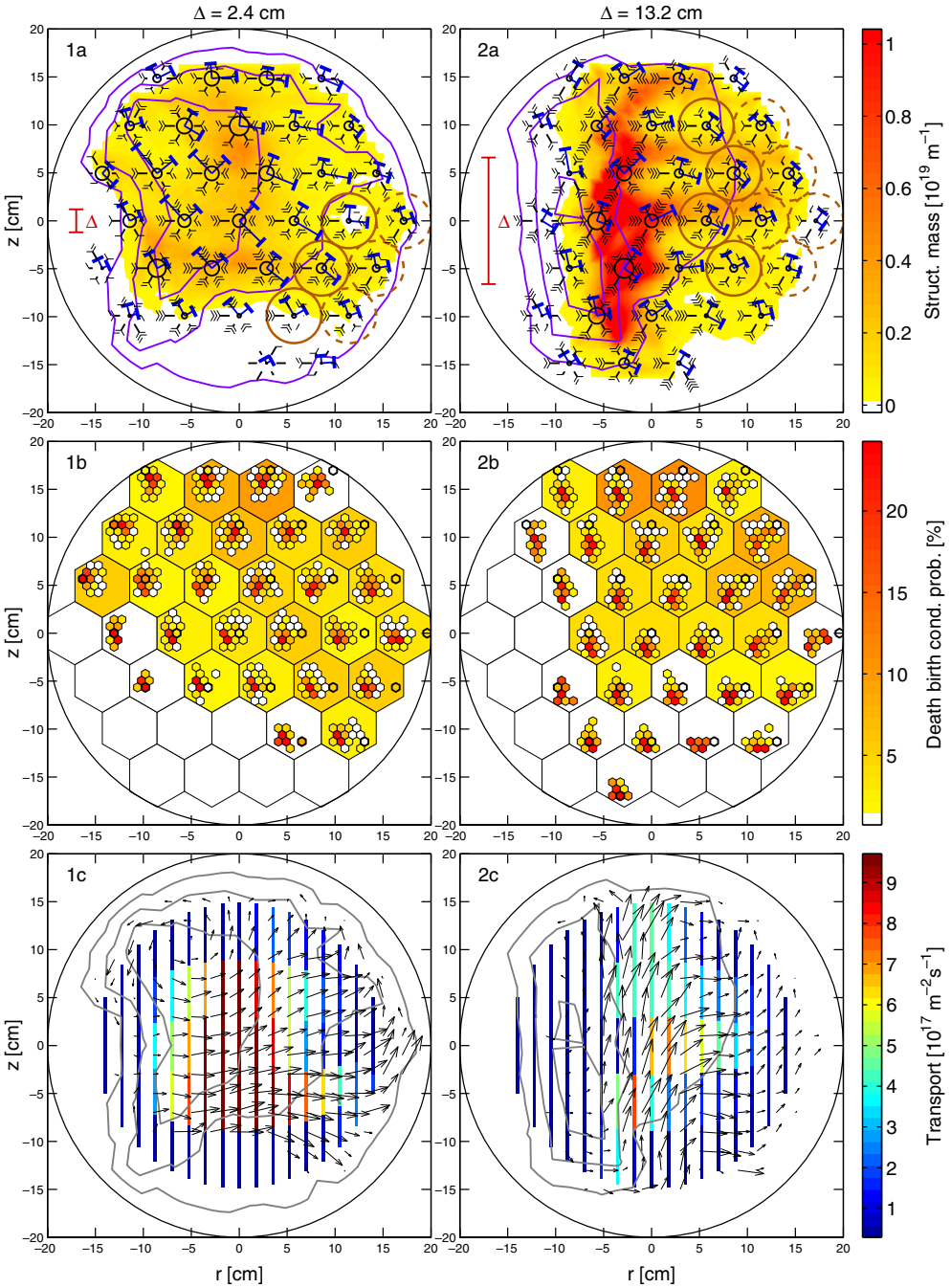

Figure 6. Comparison of positive structures and blobs in the drift-interchange-dominated (1) and interchange-dominated (2) regime. (*a*) Pilot chart. Two sets of comparable regions relative to the background density profile (contours) are highlighted by full and dashed circles, respectively. (*b*) Death–birth conditional probability. (*c*) Transport analysis. The employed representations are explained in detail in appendix A.

In the far SOL (dashed circles), the probabilities for radially-outward and radially-outward upward motion are about equal (each ∼40%), with velocities decreasing to the 750–1250 range. The structure sizes ('L' symbols) are also about equal. In conclusion, the presented data do not suggest a significant difference in the blob propagation properties in the two cases.

The death–birth conditional probability chart in figure 6(*b*) highlights that most blobs in the drift-interchange regime originate from the 'source' region [19], shown in figure 5(*a*), while most blobs in the interchange regime are born in the vicinity of $r = -5$ cm, vertically about 10 cm lower than their final destination, which is consistent with the sequence shown in figure 3. The transport chart, shown in figure 6(*c*) for positive structures only, shows that transport is predominantly radial on the LFS and comparable in magnitude for the two regimes. The vertical flux of positive structures in the interchange case is largely canceled by the contribution of negative structures in the wave-like arrangement [24]. In the drift-interchange case, the highest time-average radial transport is not caused by the largest blobs below the equatorial plane, but by smaller, more frequent events above the equatorial plane.

3.1. Comparison with numerical simulations

In the following, we bring our experimental results in the context of numerical simulations [16], which predict that two-dimensional simple magnetized toroidal plasmas go into an 'H-mode' regime when decreasing Δ and/or increasing the temperature source strength S_T, in which the blob activity is suppressed by the emergence of strong sheared $\boldsymbol{E} \times \boldsymbol{B}$ flows.

The experiments reported in this paper, in which Δ has been scanned over the full accessible range $0 \leqslant \Delta \lesssim 2a$ (shown for $0 \leqslant \Delta \lesssim a$), have not resulted in the identification of such a plasma state. Figure 4 shows that, when decreasing Δ, the plasma stays in the 'L-mode' configuration until $\Delta \simeq 8$ cm and then seamlessly transits into the fully three-dimensional drift-interchange regime, which is characterized by blobs and bursty radial dynamics in fully three-dimensional patterns (figures 5 and 6). The assumption of two-dimensional dynamics in the simulation is therefore violated, such that the predictions do not apply and a comparison cannot be meaningful.

4. Interchange nature of blobs

We now return to the discussion of the experimental results. The data presented so far have not suggested a fundamental difference between the blobs in the drift-interchange and interchange regimes, which could not be attributed to the different shapes of the background density profile. In the following, we will show that during the ejection of a blob, the phase shift between density and potential is $\pi/2$ in all cases, demonstrating the interchange nature of the blobs in both regimes.

The necessary measurements of synchronized density and potential profiles are obtained by taking subsequent shots with the HEXTIP probe array in ion saturation current and floating potential mode, respectively. A reference probe measuring ion saturation current is located in the far SOL at a toroidal separation of 90°. Trigger events, obtained when the signal on the reference probe exceeds 3.5σ, are used to generate synchronized conditionally averaged sequences of density and floating potential fluctuations.

We assume that temperature fluctuations can be neglected to compute $\tilde{\boldsymbol{v}}_{\boldsymbol{E}\times\boldsymbol{B}} \approx (\boldsymbol{B} \times \nabla\tilde{\phi}_{\mathrm{fl}})/B^2$, which we justify *a posteriori* by the excellent agreement of the flow field obtained in this way with the observed structure motion (figures 7, 8). It is worth noting that the fluctuating flow field $\tilde{\boldsymbol{v}}_{\boldsymbol{E}\times\boldsymbol{B}}$ derived from the floating potential $\tilde{\phi}_{\mathrm{fl}}$ agrees at least as well with

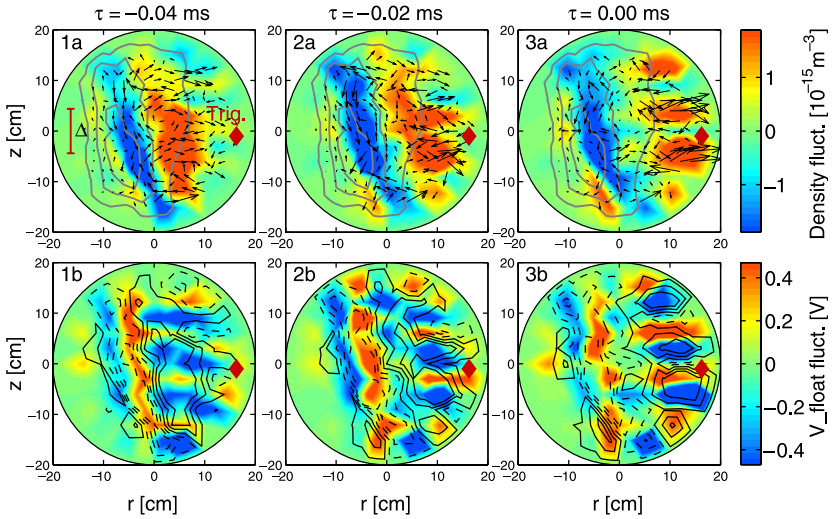

Figure 7. Time line of the interchange instability for $\Delta = 8.8$ cm for three lag times τ. (*a*) Density fluctuations and $\boldsymbol{E} \times \boldsymbol{B}$ velocity fluctuations (arrows). (*b*) Floating potential fluctuations and density fluctuations (contours).

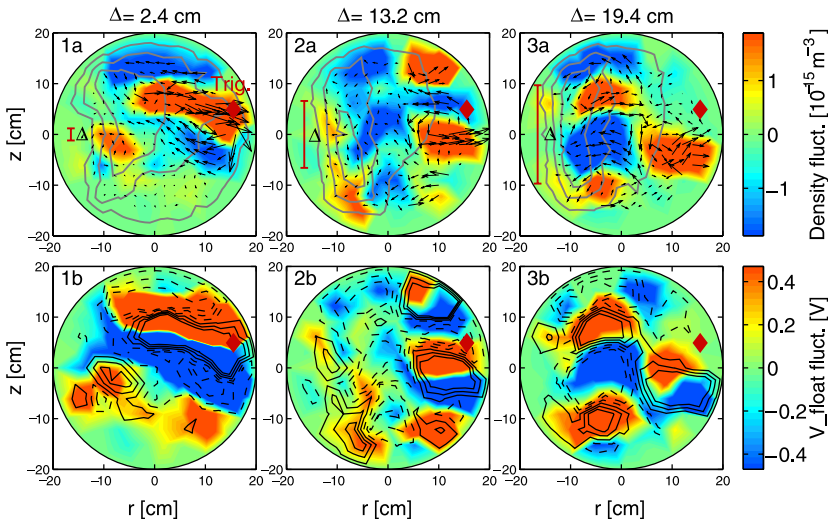

Figure 8. Conditional snapshots for different Δ for $\tau = 0$ (representation as in figure 7).

the observed structure motion than that obtained by a more complicated method that attempts to take T_e fluctuations into account by applying conditional averaging to swept Langmuir probes [30, 31], assuming that the relation $\phi = \phi_{fl} + \mu T_e$ holds for the plasma potential ϕ (μ is a constant factor).

Figure 7 shows a particularly clear sequence of how the interchange instability leads to the formation of fingered structures and wave-like patterns, qualitatively similar to the results of numerical simulations in [9, 12]. In frame (1), a large density structure remains still whole while the potential has already formed a pattern of alternating structures leading to heavily sheared $\boldsymbol{E} \times \boldsymbol{B}$ flows. Twenty microseconds later in frame (2), the density structure

is visibly deformed under the action of the alternating $\boldsymbol{E} \times \boldsymbol{B}$ flows, which have become stronger in magnitude. Another 20 μs later in frame (3), the inward going flows have locally depleted the density, which now forms a perfect alternating pattern as well, shifted with respect to the potential by $\pi/2$. This mechanism, in various guises, appears to be the fundamental driving mechanism leading to both the emergence of wave-like structures and blobs on the TORPEX low-field side. The steady-state sheared vertical $\boldsymbol{E} \times \boldsymbol{B}$ flows, which are most likely caused by independent physics related to the plasma production scheme, do not appear to play a fundamental role for the emergence of blobs. Their effect is only visible in the regime of very large Δ's, of the order of $\Delta \gtrsim a/2$, as will be shown in the following.

Figure 8 shows the conditionally averaged density and potential patterns at zero time lag, for the three studied values of Δ. A phase shift of $\pi/2$ between density and potential is evident in all cases (figure 8(*b*)), proving the interchange nature of the blobs in both the drift-interchange and the interchange regime. For the $\Delta = 19.4$ cm case (figure 8(3)), it is evident that the potential aligns well with the density in the wave region at a phase shift close to zero. Thus the self-generated $\boldsymbol{E} \times \boldsymbol{B}$ flows mostly act to make the structures rotate like vortices, and only to a limited degree drive the interchange motion as in figure 7. This inefficiency of the interchange mechanism in this scenario allows steady-state vertical $\boldsymbol{E} \times \boldsymbol{B}$ shear flows to play a role by separating off the outer parts of the wave-like structures, as shown in figure 8(3) and described in [30, 36].

5. Blobs without a ∇B-driven interchange instability: CSDX

Having demonstrated the interchange nature of blobs in TORPEX in all regimes, the question arises as to whether this conclusion also applies to blobs in linear devices, for which no ∇B-driven interchange instability exists, but which are characterized by strongly rotating plasmas in which centrifugal forces might trigger interchange instabilities. In the following, we present fast-camera and Langmuir probe measurements of the blob-ejection process in the linear device CSDX (length $L = 2.8$ m, radius $a = 0.1$ m) [33, 34], which reveal several features in support of this hypothesis. In CSDX, a helicon antenna of 5 cm radius is used to produce very dense argon plasmas ($n \sim 10^{19}\,\mathrm{m}^{-3}$, $T_\mathrm{e} \sim 2$–4 eV) immersed into an axial magnetic field of 0–100 mT. The field lines terminate in isolating surfaces on both ends of the device, with a full-size window mounted at the downstream end. The device is equipped with radially movable Langmuir probe arrays and a 28 cm Schmidt–Cassegrain telescope for optical measurements with fast cameras.

For the results presented in the following, the magnetic field was chosen as 70 mT, comparable to the value of the toroidal magnetic field in TORPEX of 76 mT, and the neutral gas pressure was 3.2 mTorr. Behind the telescope, a 14-bit Phantom 7.3 camera was operated with 96×96-pixel resolution and 8.5 μs sampling interval. Conditional averaging was applied to a sequence of 150 000 frames (total length 1.275 s), using the pixel with the highest skewness ($S \sim 2$) as a trigger signal. For a trigger level of 3.5σ, 101 non-overlapping events were detected. The resulting conditionally averaged sequence is shown in figure 9, adopting a rotating frame of reference $\boldsymbol{x}'(\tau) \equiv \boldsymbol{R}(\Omega\tau) \cdot \boldsymbol{x}$, where $\boldsymbol{R}(\Omega\tau)$ is a rotation matrix and $\Omega = -2.12$ rounds ms^{-1}, corresponding to the average clockwise rotation frequency of the dominant $m = 1$ mode [5]. An apparent counter-clockwise rotation in figure 9 thus corresponds to a deceleration with respect to Ω while an apparent clockwise rotation corresponds to an acceleration.

In frames 2–4, about 0.5 ms before the blob detection, an $m = 1$ mode appears statically in the rotating frame, meaning that it revolves with angular frequency Ω in the lab frame. At about

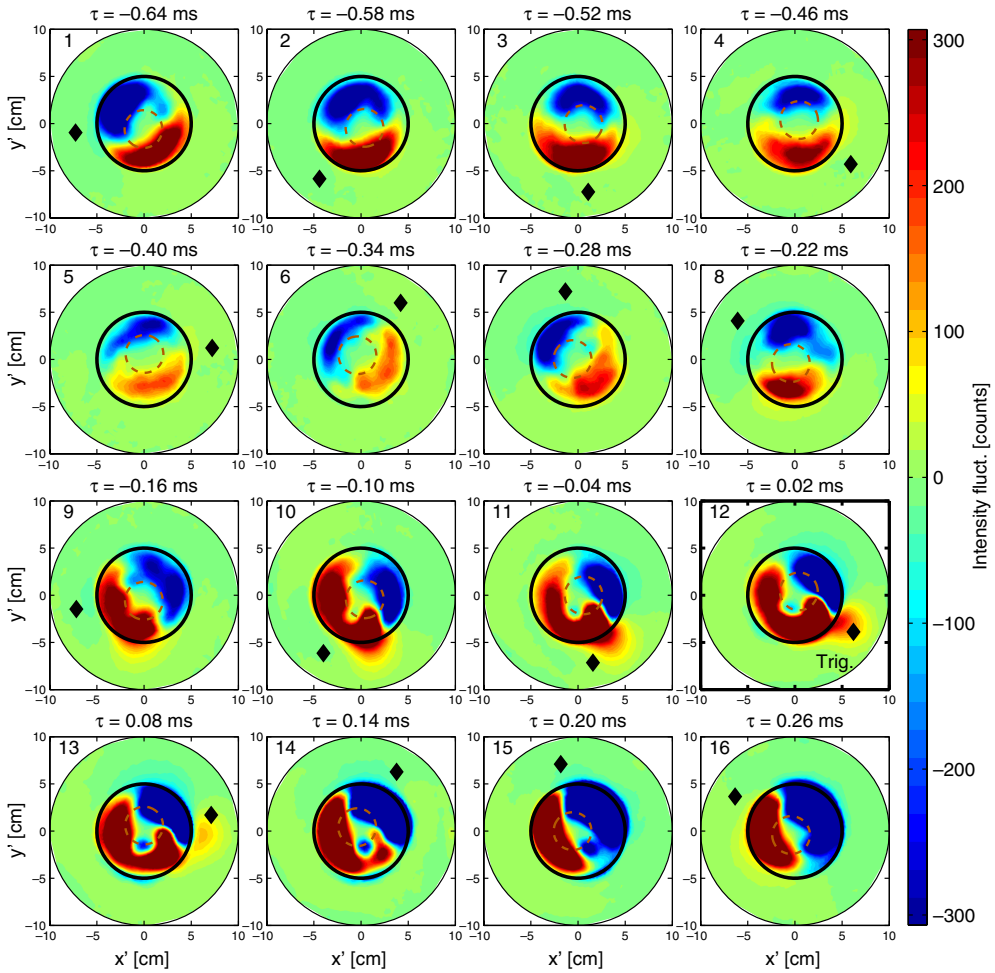

Figure 9. Conditionally averaged sequence of fast-camera data showing the ejection of a blob in the linear device CSDX. A rotating frame of reference is used (frequency $\Omega = -2.12$ rounds ms^{-1}), coinciding with the lab frame at zero time lag τ (highlighted frame). A full-size telescope was used to essentially eliminate perspective distortions. The telescope's secondary mirror causes a blind spot, in which the intensity is significantly reduced (dashed circle). The inner and outer circles represent the plasma source and the vacuum vessel, respectively.

0.4 ms before the detection (frames 4–6), the conditionally averaged signal loses significantly in amplitude, which could mean either a reduction of the mode amplitude or a decorrelation caused by incoherent changes of the mode structure, or both. The $m = 1$ structure decelerates significantly in frames 4–6. From frames 7 to 9 the mode structure accelerates strongly, going along with an increase of the conditionally averaged signal. In frame 9, the ejection of the blob starts from the rear end of the positive crest while the mode still grows. As soon as the blob extends out of the main plasma region into the cold neutral gas of the SOL, its azimuthal motion is heavily braked (frames 9-13). The radial velocity of the blob appears to decrease proportionally to its azimuthal velocity, with the radial motion essentially stopping in frame 13, where the blob is finally fully sheared off the crest. The blob dissipates away quickly (frames 13–14), well before it could reach the wall. In frames 15–16, the $m = 1$ structure reforms and continues to rotate with frequency Ω.

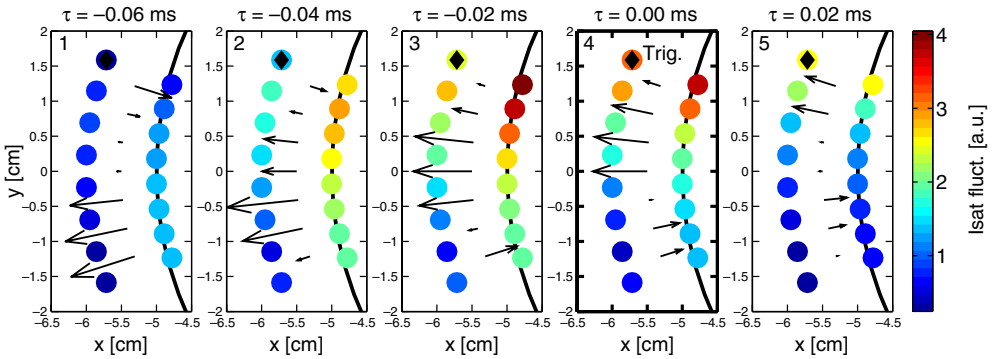

Figure 10. Conditionally averaged blob-ejection sequence observed with a Langmuir probe array consisting of three arcs of eight tips each, operated in I–V–I configuration. The I_{sat} measurements of the inner and outer arcs are shown as color-coded dots. The radial $\boldsymbol{E} \times \boldsymbol{B}$ velocities obtained from the V_{float} measurements of the middle arc are shown as arrows. A trigger condition of 3.5σ was used. One observes that the ejection of the blob is accompanied by a burst in the radial $\boldsymbol{E} \times \boldsymbol{B}$ velocity.

To complement these results with density and $\boldsymbol{E} \times \boldsymbol{B}$-flow measurements, we use a Langmuir probe array consisting of three arc-shaped rows, separated radially by 0.5 cm, each equipped with eight azimuthally separated tips. The array is positioned on the left-hand side in the view of figure 9, such that the inner row coincides with the source radius of 5 cm, resulting in the arrangement shown in figure 10. The inner and outer rows measure ion saturation current while the middle row is used to obtain the radial $\boldsymbol{E} \times \boldsymbol{B}$ velocity from floating potential measurements. Maximum cross-correlations between the probes and camera pixels are typically 0.4–0.45 [5]. Although the probe array covers only a region of about $2 \times 4\,\mathrm{cm}^2$, which is comparable to the size of the conditionally averaged blob in figure 9, the fact that the blob passes by the probe array in rapid azimuthal rotation helps to infer its macroscopic properties.

Figure 10 shows the conditionally averaged blob-ejection sequence as seen by the probe array in the lab frame, triggered when the signal of the outermost topmost Langmuir probe, which is located about 1 cm in the SOL region, exceeds 3.5σ, which we interpret as a blob event. The sequence shows that the observation of a blob occurs shortly after the positive mode structure passes in the core plasma (frames 2–3), which also increases in amplitude before the ejection (frame 3). Frames 3 and 4 show that there is no plasma coming from the azimuthal direction which could explain the density rise at the trigger location, which must therefore result from radial dynamics. This is consistent with the observation of a burst in the radial $\boldsymbol{E} \times \boldsymbol{B}$ velocity before the blob is detected (frames 1–4). Although the radial velocity burst comes slightly too late to fully explain the density rise in the SOL, it is still consistent with the picture that the blob is generated by in-phase bursts of density and radial $\boldsymbol{E} \times \boldsymbol{B}$ velocity.

In conclusion, three indications exist that a rotation-driven interchange instability plays a role for the ejection of blobs in the linear device CSDX: (1) An acceleration of the $m = 1$ mode is observed preceding the blob-ejection, which would temporarily increase the effective gravity force, destabilizing the interchange instability. (2) A rise in both density and light intensity is observed to precede the blob-ejection, which would cause a steepening of the density gradient, further destabilizing the interchange instability. (3) A burst of radial $\boldsymbol{E} \times \boldsymbol{B}$ velocity occurs roughly in phase with the density burst, corresponding to a phase shift between density and potential of about $\pi/2$, signature of an interchange mode. In addition, the fact that the radial

propagation of the blobs stagnates once the azimuthal momentum is lost is consistent with the picture that polarization due to an effective gravity force determines the blob propagation [7]. It is therefore possible that the physics of the blobs in CSDX is the same as in TORPEX, if the constant ∇B driving term is replaced by a time-dependent driving term given by the centrifugal force. More detailed investigations of this are subject to ongoing research and will be published separately.

6. Summary and conclusions

In this paper, we have established that the previously published measurements of plasma blobs in the TORPEX interchange-dominated regime in helium and in hydrogen are well comparable. The onset of blobs has been studied as a function of the field-line-return distance Δ and the observation of blobs has also been reported in the drift-interchange-dominated regime characterized by $\Delta < 8\,\mathrm{cm}$.

Despite the fact that these blobs are inherently three-dimensional structures, which are disconnected from the plasma sheath, they exhibit similar statistical properties as the sheath-connected blobs in the interchange regime. It is concluded that it does not seem to matter whether the blobs are actually connected to the plasma sheath at a material surface (a conductor) or lose their defining structure after a similar parallel distance within the plasma (another conductor). This may suggest that a closure model similar to the sheath-closure [8, 9, 12, 13] might be developed for the situation where the blob terminates within the plasma, but ultimately three-dimensional models as in [17] are necessary to determine the parallel extensions of the blobs and their propagation properties self-consistently.

A prediction based on numerical simulations in [16] that two-dimensional simple magnetized toroidal plasmas go into an 'H-mode' regime if Δ is decreased below a certain threshold was experimentally investigated. We could not identify such a plasma state and found instead that the plasma turbulence seamlessly assumes an increasingly three-dimensional character as Δ is decreased, violating the assumption of two-dimensional dynamics in the simulation.

Using spatially resolved density and potential measurements, the entire time line of an interchange instability leading to the formation of wave-like structure patterns and blobs could be directly observed for the first time. The results show that a background $\boldsymbol{E} \times \boldsymbol{B}$ shear flow is not essential for the generation of blobs, which plays a role only for $\Delta \gtrsim a/2$ in TORPEX, as discussed in detail for $\Delta = 19\,\mathrm{cm}$ in [30, 36]. It was further shown that the phase shift between density and potential fluctuations during the generation of blobs is $\pi/2$ in all studied cases, demonstrating the interchange nature of the blobs.

We have further investigated the generation of blobs in the linear device CSDX, in which a ∇B-driven interchange instability is absent. The presented fast-camera and Langmuir probe measurements of the blob-ejection process demonstrate that both an increase in intensity and an acceleration of the $m = 1$ mode structure precede the ejection of a blob, which is accompanied by an in-phase burst of the radial $\boldsymbol{E} \times \boldsymbol{B}$ velocity, corresponding to a phase shift between density and potential of about $\pi/2$. These results support the hypothesis that an interchange instability driven by centrifugal forces might be responsible for the generation of blobs in the linear configuration. It is therefore possible that a unified picture of interchange-driven turbulence can account for both the TORPEX and CSDX observations of turbulence and blobs, where the main driving term comes from ∇B in the toroidal geometry and from time-dependent centrifugal forces in the linear configuration. If this possibility finds further supporting evidence, it is then very likely that the picture also applies to tokamaks, in which both driving mechanisms are strongly present.

To further improve our understanding of the physics of blobs, we plan to install a large probe array in the CSDX device to obtain a more global picture of the plasma dynamics from probe measurements, which is an indispensable complement to understand many features in the fast-camera data that we can currently not explain.

Acknowledgments

This research was partly funded by the Fonds National Suisse de la Recherche Scientifique and was partly performed under US Department of Energy DOE Grant No. DE-FG02-06ER54871. Fruitful discussions with J Boedo, A Diallo and P Ricci are gratefully acknowledged.

Appendix A. Representations for probabilistic structure-analysis results

In this appendix, we explain several representations in detail that have been developed to graphically represent the probabilistic properties of turbulent structure trajectories, as obtained from a pattern-recognition based analysis approach such as presented in [28].

Appendix A.1. Pilot chart

The pilot chart (figure 6(*a*)) is a representation suitable to represent the angle distributions of a two-dimensional vector field, which was inspired by wind roses in nautical navigation charts. Each rose is representative of a square or hexagonal region, in which the probability distribution of propagation directions is estimated from the observed trajectories. Usually eight or six direction intervals are distinguished, for which the probability is encoded as the relative length of arrow shafts. The average speed in each direction is encoded as the number of feathers (1–8), each standing for $250\,\mathrm{m\,s^{-1}}$ unless noted otherwise. The area of the circle in the center of each rose is proportional to the number of trajectory realizations, thus is a measure of the statistical accuracy. On top of each rose, 'L' symbols code the typical structure sizes and orientations in this region, obtained from second-order geometrical moments [28].

Appendix A.2. Conditional probability chart

This representation addresses the conditional probability that event B (e.g. the birth of a structure) occurs in a certain spatial region, given that event A (e.g. the death of a structure) occurs in another (or the same) region (figure 6(*b*)). The results are coded as the colors of a grid of small hexagons inside a grid of large hexagons. One looks up the position of event A in the large hexagons and interprets the interior as a self-similar copy of the whole domain. One then finds the position of event B inside this large hexagon and looks up the conditional probability $p(B|A)$. To facilitate the orientation, a black frame is drawn around the small hexagon corresponding to the position of the event A itself. The background colors of the large hexagons represent the probability that event A occurs in this region.

Appendix A.3. Transport chart

The transport chart (figure 6(*c*)) represents the structure-induced transport through a grid of test surfaces. Each time a structure center of mass crosses a surface, a 'transport event' is recorded, consisting of the crossing time and the transported structure mass. After an observation time τ, the signed sum of all transported mass is calculated and divided by τ and the area of the test surface. This gives the transport in units of particles $\times\ \mathrm{s^{-1}\,m^{-2}}$, which is represented as a

color-coded bar at the position of the test surface. The over plotted vector field is the ensemble-averaged flux density $\langle\bar{\Gamma}\rangle \equiv \langle\bar{n}\boldsymbol{v}\rangle$, where $\bar{n} \equiv \int_S \mathrm{d}^2\sigma\, n(x, y)/\int_S \mathrm{d}^2\sigma$ is the average density of the structure, $\boldsymbol{v}$ is the structure velocity and $\langle\cdot\rangle$ is an ensemble average over all structure realizations. Long arrows thus mean that the average structure causes large transport, not that the transport in a time-average sense is large at this position. Figure 6(1*c*) represents a case where the position of the largest time-average transport does not coincide with the position where the transport caused by a typical structure is largest.

References

[1] Zweben S J *et al* 2007 *Plasma Phys. Control. Fusion* **49** S1
[2] Ramisch M *et al* 2005 *Phys. Plasmas* **12** 032504
[3] Carter T A 2006 *Phys. Plasmas* **13** 010701
[4] Windisch T, Grulke O and Klinger T 2006 *Phys. Plasmas* **13** 122303
[5] Antar G Y, Yu J H and Tynan G R 2007 *Phys. Plasmas* **14** 022301
[6] Katz N *et al* 2008 *Phys. Rev. Lett.* **101** 015003
[7] Krasheninnikov S I 2001 *Phys. Lett.* A **283** 368
[8] D'Ippolito D A, Myra J R and Krasheninnikov S I 2002 *Phys. Plasmas* **9** 222
[9] Yu G Q and Krasheninnikov S I 2003 *Phys. Plasmas* **10** 4413
[10] Garcia O E, Naulin V, Nielsen A and Rasmussen J J 2004 *Phys. Rev. Lett.* **92** 165003
[11] Bisai N *et al* 2005 *Phys. Plasmas* **12** 072520
[12] Yu G Q, Krasheninnikov S I and Guzdar P N 2006 *Phys. Plasmas* **13** 042508
[13] Garcia O E, Bian N H and Fundamenski W 2006 *Phys. Plasmas* **13** 082309
[14] Naulin V 2007 *J. Nucl. Mater.* **363–365** 24–31
[15] Holland C *et al* 2007 *Plasma Phys. Control. Fusion* **49** A109
[16] Ricci P, Rogers B N and Brunner S 2008 *Phys. Rev. Lett.* **100** 225002
[17] Naulin V, Windisch T and Grulke O 2008 *Phys. Plasmas* **15** 012307
[18] Windisch T, Grulke O, Schneider R and Kervalishvili G N 2008 *Contrib. Plasma Phys.* **48** 58
[19] Fasoli A *et al* 2006 *Phys. Plasmas* **13** 055902
[20] Podestà M *et al* 2005 *Plasma Phys. Control. Fusion* **47** 1989–2003
[21] Müller S H *et al* 2004 *Phys. Rev. Lett.* **93** 165003
[22] Müller S H *et al* 2005 *Phys. Plasmas* **12** 090906
[23] Poli F M, Ricci P, Fasoli A and Podestà M 2008 *Phys. Plasmas* **15** 032104
[24] Müller S H *et al* 2007 *Phys. Plasmas* **14** 110704
[25] Boedo J A *et al* 2003 *Phys. Plasmas* **10** 1670–7
[26] Garcia O E *et al* 2006 *Plasma Phys. Control. Fusion* **48** L1–10
[27] Labit B *et al* 2007 *Plasma Phys. Control. Fusion* **49** B281
[28] Müller S H *et al* 2006 *Phys. Plasmas* **13** 100701
[29] Podestà M *et al* 2008 *Phys. Rev. Lett.* **101** 045001
[30] Furno I *et al* 2008 *Phys. Rev. Lett.* **100** 055004
[31] Furno I *et al* 2008 *Phys. Plasmas* **15** 055903
[32] Theiler C *et al* 2008 *Phys. Plasmas* **15** 042303
[33] Tynan G R *et al* 2004 *Phys. Plasmas* **11** 5195
[34] Burin M J *et al* 2005 *Phys. Plasmas* **12** 052320
[35] Müller S H *et al* 2009 Source formulation for electron-impact ionization for kinetic and fluid plasma simulations *Plasma Phys. Control. Fusion* to be submitted
[36] Diallo A *et al* 2008 *Phys. Rev. Lett.* **101** 115005